

Geophysical Research Letters®

RESEARCH LETTER

10.1029/2021GL095133

Key Points:

- The CE-4 LPR reveals the paleo-surface of the lunar farside at a depth between 7 and 20 m
- The LPR has mapped a 270 m sized buried crater probably related to a larger circular depression on the lunar surface
- The geomorphology, the subsurface structure, the impact melt deposits, and the exposure time of the buried crater, are analyzed

Supporting Information:

Supporting Information may be found in the online version of this article.

Correspondence to:

Y. Xu,
yixu@must.edu.mo

Citation:

Lai, J., Xu, Y., Bugiolacchi, R., Wong, H. K., Xu, L., Zhang, X., et al. (2021). A complex paleo-surface revealed by the Yutu-2 rover at the lunar farside. *Geophysical Research Letters*, 48, e2021GL095133. <https://doi.org/10.1029/2021GL095133>

Received 14 JUL 2021

Accepted 24 SEP 2021

A Complex Paleo-Surface Revealed by the Yutu-2 Rover at the Lunar Farside

Jialong Lai^{1,2} , Yi Xu¹ , Roberto Bugiolacchi^{1,3} , Hon Kuan Wong¹, Luyuan Xu¹ , Xunyu Zhang¹ , Ling Zhang¹, Xiaoping Zhang¹ , Long Xiao⁴ , Bin Liu⁵, and Kaichang Di⁵ 

¹State Key Laboratory of Lunar and Planetary Sciences, Macau University of Science and Technology, Macau, ²School of Science, Jiangxi University of Science and Technology, Ganzhou, China, ³University College London, Earth Sciences, London, UK, ⁴School of Earth Sciences, Planetary Science Institute, China University of Geosciences, Wuhan, China, ⁵State Key Laboratory of Remote Sensing Science, Institute of Remote Sensing and Digital Earth, Chinese Academy of Sciences, Beijing, China

Abstract The observable lunar surface is represented by a ubiquitous layer of fine-grained materials produced by billions of years of hypervelocity pounding of its crustal layer. The data from the Lunar Penetrating Radar onboard Chang'e-4 (CE-4) rover (Yutu-2), which is exploring the Von Kármán Crater on the lunar farside, are helping to peel back the upper layer of finely comminuted materials, interpreted as a thick layer of ejecta from the neighboring Finsen crater, to reveal a complex paleo-surface morphology. During the rover's 560 m journey, from depths of 7–20 m, distinct variations in the returned signal characteristics reveal a possible 270 ± 10 m buried crater with an estimated age of less than 100 m.y. A smooth surface depression that lies to the southwest of the Yutu-2 rover's travel path might not be the remnant of a degraded crater but a related surface expression of the hidden structure.

Plain Language Summary The absence of an atmosphere and substantial resurfacing events in the last couple of billion years means that the Moon's surface has journeyed through space exposed to anything that travels through it and, unlike the Earth, most of these “encounters” have left a mark. Thus, the good news for scientists is that the lunar surface represents a record of astrophysical phenomena within the Solar System that is no longer available on its larger companion: our planet. However, the larger impacts have indeed contributed to modify its surface hiding some of its old terrains. The Lunar Penetrating Radar (LPR) onboard Chang'e-4 (CE-4) rover (Yutu-2) can see below the surface as it makes its way across the lunar ground, revealing the ancient lunar surface (paleo-surface) at the depth of ~12 m. It has mapped its elevation profile, which now we can see that it has been substantially modified following its formation some 3.1 billion years ago. Notably, the LPR has discovered a 270 m sized buried crater corresponding to a large ground depression seen on the surface, a first achievement for lunar radar sounding.

1. Introduction

Impact craters represent the most salient geomorphological characteristic of the lunar surface and are a key to a better understanding of the geology of our satellite. Crater chronology, a dating methodology derived from returned lunar samples, remains the sole remote sensing methodology for estimating absolute surface ages across the solar system. The geomorphology of craters can constrain their age and shed light on the regional stratigraphy, set constraints on the thickness of lunar regolith, and assist in estimating the depth of the basalt layers. The impact events also exhume materials from depth granting access to analysis. However, the relentless reworking of the surface, from the micro to the macro level, remodels the lunar surface through a process of destruction and burial (Carrier et al., 1991). Gravity field variations interpreted from the GRAIL data (Evans et al., 2016; Sood et al., 2017) have revealed tens to hundreds of km sized craters hidden below the lunar maria. Ground Penetrating Radars (GPR) can reveal the shallow subsurface stratigraphy, including buried craters, and they have been deployed on Earth, Mars, and the Moon. On our planet, the scientific yield has been modest probably due to the high attenuation of GPR signals in moist environments and interferences caused by vegetation and human activities (Heggy & Paillou, 2006). On Mars, the dense data coverage of the Shallow Radar (SHARAD) sounder in the polar region enables a three-dimensional view of hidden structures and reveals a couple of km-scale buried craters (Putzig et al., 2018). However, due to their limited spatial resolution, SHARAD and GRAIL are not suitable for detecting small-scale and close-to-surface geological discontinuities.

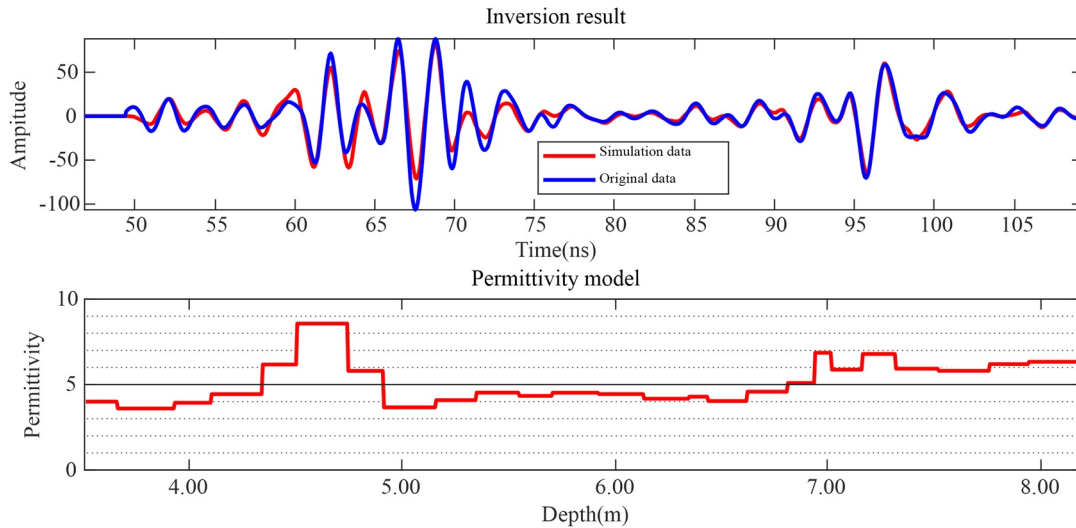


Figure 1. Permittivity profile estimated with deconvolution method.

The Lunar Penetrating Radar (LPR) onboard Chang'e-4 (CE-4) rover (Yutu-2) has been surveying the shallow subsurface around its landing site on the lunar farside for over 2 years. It shows the stratigraphic structure up to 330–500 m deep (Lai et al., 2020; J. Zhang, Xu, et al., 2021), including a ~12-m thick regolith layer (Guo et al., 2021; Lai et al., 2019; Li et al., 2020; L. Zhang, Xu, et al., 2021), the basalt layers deposited by multiple lava eruption events (Lai et al., 2020; Yuan et al., 2021; L. Zhang et al., 2020), and evidence for surface modification events that occurred in the Von Kármán crater (VK) inside the South Pole-Aitken (SPA) basin (Lu et al., 2021; Qiao et al., 2019; Xiao et al., 2021; Xu et al., 2021) (Figure S1). Here, we report the discovery of a 270-m sized buried crater with clear diagnostic geomorphological features on the lunar farside using LPR data from the first 25 lunar days of the CE-4 mission. The LPR also reveals the paleo-surface below the area surveyed by the Yutu-2 rover at the depth of about 12 m that was exposed at a time before the Finsen ejecta deposition (Huang et al., 2018).

2. Methods

The LPR detected a continuous subsurface reflector at the depth of ~12 m, which has been subsequently interpreted as the lower interface of the fine-grained lunar regolith layer (Guo et al., 2021; Lai et al., 2019, 2020). As the Yutu-2 rover exploration journey progressed (Figure 2), the reflector's signal has increased in depth for then reaching a plateau (details in Section 3), drawing what appears to be the outline of a small basin, probably an impact crater. Further, the radar signal strength and pulse width changed when the rover moved from the outside of the alleged crater to the rim (Figure 3b), indicating that the dielectric properties of materials outside the crater are different from those on the crater walls. To test this hypothesis, we applied two methods to estimate the permittivity value of the materials.

2.1. Permittivity Value Estimation With Deconvolution Method

The normalized waveform of the output pulse of LPR CH-2 antenna $w(t)$ is obtained based on the permittivity value of rock samples of Apollo missions and received waveform given in Fang et al. (2014). We assume that the received radar signal $x(t)$ is the convolution results of $w(t)$ and reflection coefficients $r(t)$ (Robinson, 1985), if noises are ignored.

$$x(t) = w(t) * r(t) \quad (1)$$

$$r(t) = \{R_1, R_2, \dots, R_n\} \quad (2)$$

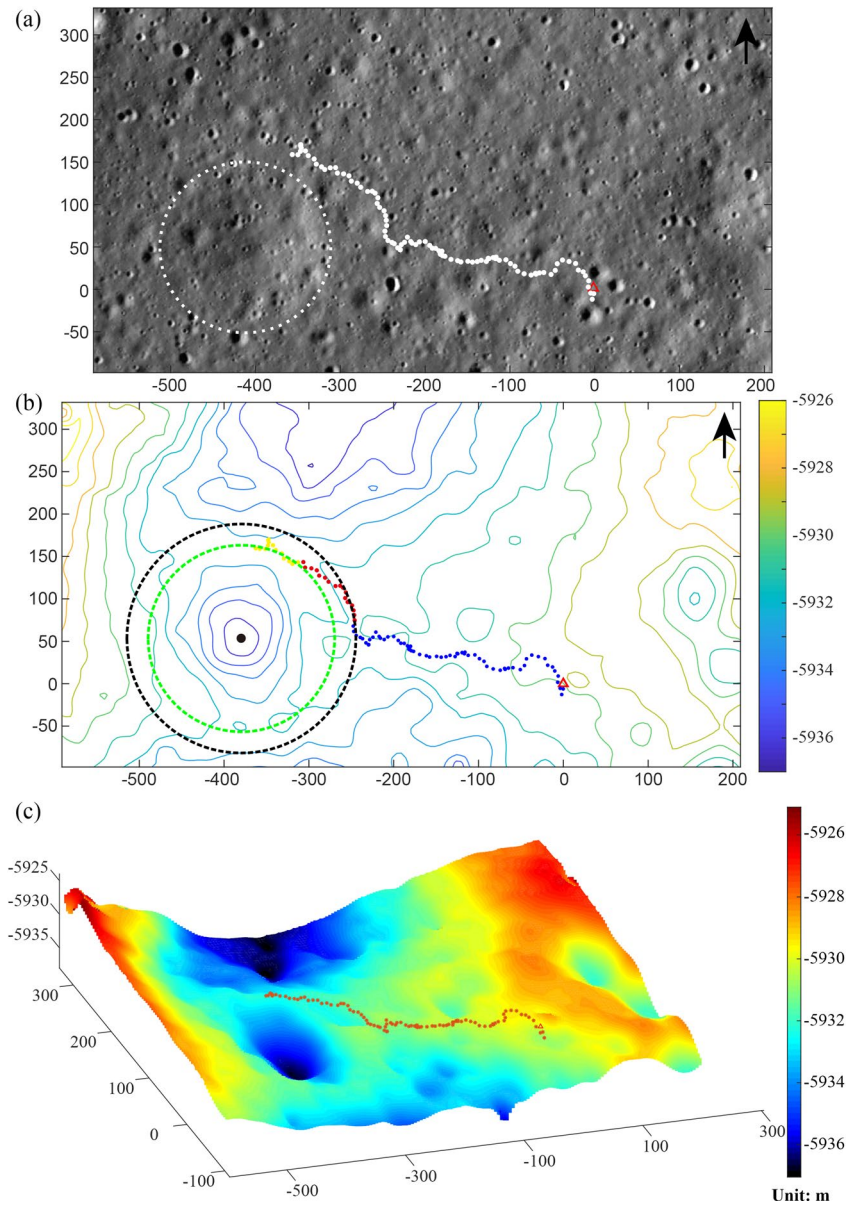


Figure 2. The first 25 lunar days traversing path of the Yutu-2 rover. (a) The LROC (Robinson et al., 2010) Narrow-Angle Camera (NAC) image of Yutu-2 rover surveying area. The black arrow indicates North. The landing site of the Chang'e-4 mission is marked by a red triangle and the waypoints of the rover's path are marked as white dots. The current cumulative length of LPR data collection is ~ 563 m. The circle indicated by the white dash line marks the outline of the depression close to the traveling path of the Yutu-2 rover (NAC image ID: M134022629LE, 1.27 m/pixel, 77.55° incidence angle); (b) In the contour plot of the CE-4 landing site, the color bar refers to the elevation in meters. The blue, yellow, and red dots represent the traveling path, and the color differences help tracing the underlying paleo-surface revealed by radar image by turning red above the descending and yellow when flat or rising. The starting and ending positions of the declining part are also marked as red and green triangles in the radar image shown in Figures 3a and 3c, respectively. (c) The 3D view of the surveying area. Surface DEM data were derived from Lunar Reconnaissance Orbiter (LRO) Narrow Angle Camera (NAC) stereo pair image (Robinson, 2019). The unit of X,Y axle and color bar are in meters.

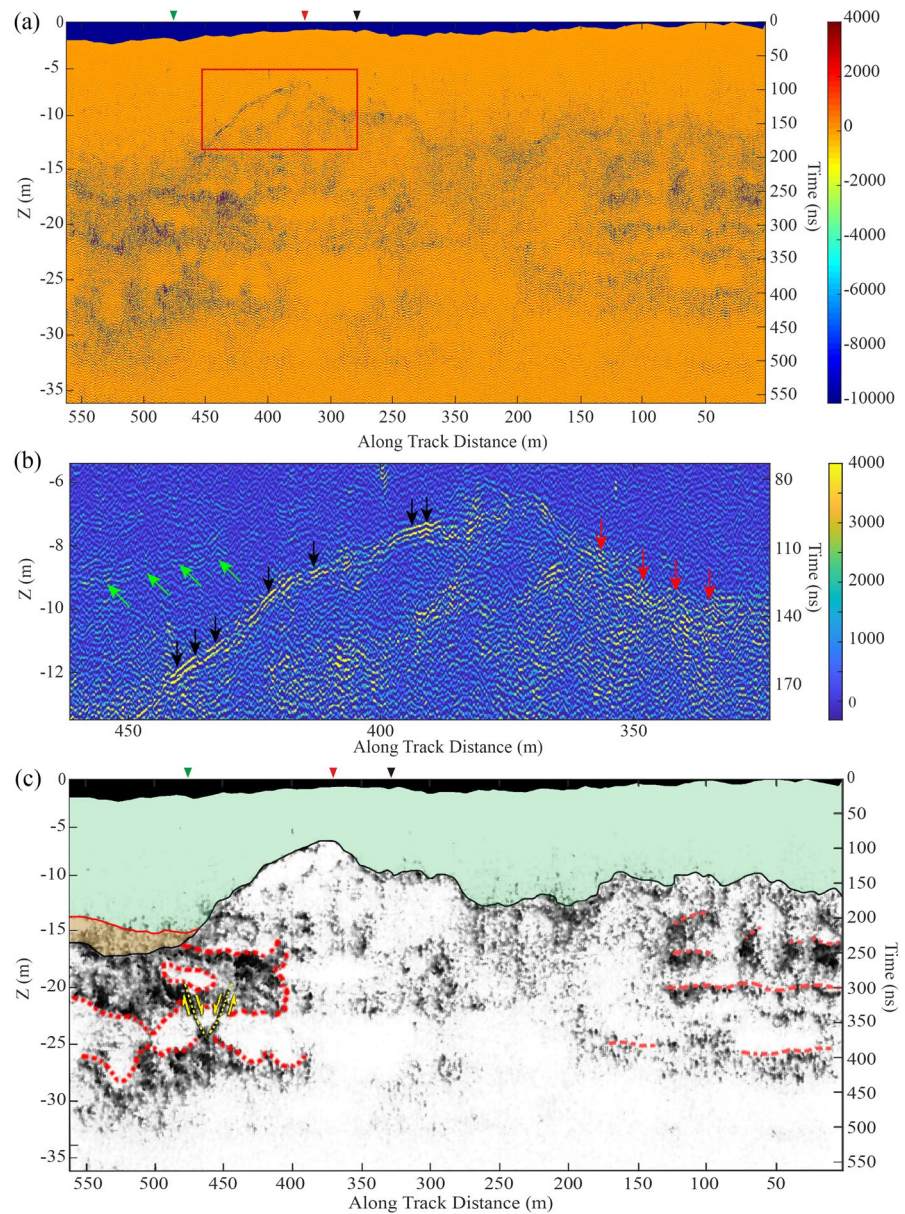


Figure 3. Processed Lunar Penetrating Radar results of the Chang'e-4 surveyed area. (a) Lunar Penetrating Radar results of CE-4 site of the first 25 lunar days after processing. The color bar refers to the amplitude of the radar signal. The Z position of the subsurface reflectors is converted with $\bar{\epsilon} = 4.3 (\leq 154 \text{ ns}) / 6 (>154 \text{ ns})$. The black marker above the figures shows the starting position of the rim of the buried crater, the red triangle marks the position where the subsurface reflector starts to decline, and the green triangle marks the position where the subsurface reflector flattens. (b) Enlarged radar image of the red rectangle as in Figure 3a. The color bar in (a) and (b) refers to the amplitude of the radar signal in mV. Red arrows point to a fuzzy subsurface boundary containing multiple scattering signals. Black arrows indicate that the boundary becomes clear and sharp when the traverse distance is between 390 and 440 m. Green arrows denote the continuous reflectors within the buried crater that could have been caused by the depositing events. (c) Enhanced radar image. The Green region highlights the relatively homogeneous radar reflections overlying the alleged paleo-surface. Red dashed lines mark possible disruption boundaries of plastic deformations of the rocks at depth due to the force of the impact. The yellow dashed lines represent a fault-like morphology. The brown "wedge" represents the probable accumulation of debris (scree) at the bottom of the crater. Note that the scanning sequence of the LPR shown here runs from right to left.

R_n depends on the permittivity values of neighboring layers, as follows:

$$R_n = \frac{\sqrt{\varepsilon_n} - \sqrt{\varepsilon_{n+1}}}{\sqrt{\varepsilon_n} + \sqrt{\varepsilon_{n+1}}} \quad (3)$$

Xia et al. (2004) employed the deconvolution method (Yilmaz, 2001) in inverting a series of reflection coefficients of low-loss materials using GPR data (Xia et al., 2004); however, they obtained the non-discrete reflection coefficient. In this work, we applied a genetic algorithm (Holland, 1992) to infer the discrete reflection coefficients and corresponding permittivity values. Real-coded genetic algorithms (Goldberg, 1991) and adaptive genetic algorithm (Yang et al., 2016) are adopted here. The target function is set as

$$\psi = \min(\sum |x_r(t) - x_s(t)|) \quad (4)$$

where $x_r(t)$ is the measured value obtained from LPR data and $x_s(t)$ is the inversed waveform. The target function aims to minimize the differences between the measured values and the synthetic waveform. $x_s(t)$ can be obtained from Equation 1, $r(t)$ is obtained from Equation 3, and model m of subsurface materials:

$$m = \{\varepsilon_1, \varepsilon_2, \dots, \varepsilon_n, h_1, h_2, \dots, h_n\} \quad (5)$$

where ε_n is the permittivity value of n_{th} layer and h_n is the thickness of n_{th} layer.

Here, we used radar data track No. 10976 as an example for permittivity inversion. Both the declining reflector (black arrows in Figure 3b) caused by the suspected buried crater and hyperbolic curve caused by the rock in the regolith appears in the selected radar data. The geometric spreading correction of radar signal should be considered and performed as follows:

$$A_0 = A\bar{v}te^{\alpha t} \quad (6)$$

where A_0 is amplitude after compensation, A is the amplitude of receiving signals, t is the two-way timing delay, \bar{v} is the average propagation speed of an electromagnetic wave in the subsurface materials, and α is the absorption factor, which can be expressed by 7.

$$\alpha = \pi f \tan \delta \sqrt{\varepsilon'} / c_0 \quad (7)$$

where f is the frequency of radar, $\tan \delta$ is loss tangent, c_0 is the light speed in vacuum, and ε' is the average permittivity value of materials. We assume that $\tan \delta = 0.004$, $\varepsilon' = 4$ (Lai et al., 2019) to compensate for the amplitude of the radar signal. The inversed permittivity profile is shown in Figure 1.

The upper figure shows the synthetic waveform (red) and LPR data (blue). The figure below shows the inversed permittivity profile with depth.

The inferred permittivity of the rock that results in the hyperbolic shaped signal is 8.6, while the ε' of the surface of the buried crater is 6.8, the ε' of the material below the crater is 6.

2.2. Permittivity Estimation Based on the Continuity of the Subsurface Reflector

Two continuous reflectors appear at the depth of ~ 250 ns in the radar image, indicated by the black solid line and red dash line in Figure S3a, when the aggregated traveling distance of the Yutu-2 rover is 420–480 m and 480–520 m, respectively. Although the two reflectors connect at ~ 480 m and probably are caused by the same interface, they do not follow the same trend. The main reason could be the different permittivity values of materials overlying the reflectors change the apparent depth of two reflectors in the radar image.

Therefore, we could infer the average permittivity value of materials in the area between the red dash line and the black solid line by assuming the two reflectors follow the same trend.

$$y(x) = y_1(x) + (y_2(x) - y_1(x)) * \text{sqrt}(\bar{\varepsilon}_{up} / \bar{\varepsilon}_{down})$$

where x is the horizontal distance, $y_1(x)$ is the delay of the reflector indicated by the red dash line, $y_2(x)$ is the delay of the reflector indicated by the black solid line, $y(x)$ is the modified delay based on the unknown permittivity value. $\bar{\epsilon}_{up}$ and $\bar{\epsilon}_{down}$ are average permittivity values of the materials above and below the red dash line (the surface of the buried crater), respectively. Assuming $\bar{\epsilon}_{up} = 4$, we obtained that $\bar{\epsilon}_{down} = 5.8$ (green dash line in Figure S3b) and $\bar{\epsilon}_{down} = 6.2$ (black dash line in Figure S3b). From Figure S3b, we observe the aforementioned reflector becomes straight in the region of 420–530 m when $\bar{\epsilon}_{down} = 5.8 - 6.2$. The estimated permittivity value also agrees with the result ($\epsilon = 6$) inferred with the deconvolution method. Therefore, the subsurface layer (black/green dash line) shown in Figure S3b might be a plausible geologic structure.

2.3. Pearson Correlation

We investigated whether the paleo-surface revealed by LPR correlates to the observed surface topography by using the Pearson correlation parameter. The correlation value r is obtained with the following equation:

$$r = \frac{\sum XY - \frac{\sum X \sum Y}{N}}{\sqrt{\left(\sum X^2 - \frac{(\sum X)^2}{N} \right) \left(\sum Y^2 - \frac{(\sum Y)^2}{N} \right)}}$$

X, Y are input data. For example, X, Y to calculate the correlation between the paleo-surface and surface is the elevation data of paleo-surface and surface, respectively.

3. Results and Discussions

3.1. LPR Results

The LPR employs two sets of antennae each operating at different frequencies (centered at 500 and 60 MHz). The LPR data from the higher frequency channel are used in this work, with a resolution of 0.3 m in vacuum (Fang et al., 2014), and were collected during a ~563 m long surveying path of the Yutu-2 rover. The current location of the Yutu-2 rover is close to a ~180 m diameter rounded depression, resembling a highly degraded crater (Figure 2a).

The LPR raw data underwent a series of steps, including repetitive data conditioning, noise filtering, background removal, and amplitude compensation. Details can be found in the Text S1 in Supporting Information S1.

Figure 3 shows the processed radar image and the LPR signal in the green, uppermost subsurface area (Figure 3c) to be relatively weak, indicating the materials within the region are rather homogenous and interpreted as representing the lunar regolith layer by previous studies (Lai et al., 2020; J. Zhang, Xu, et al., 2021; L. Zhang et al., 2020). The surface materials are interpreted as Eratosthenian ejecta materials, mostly originating from the nearby Finsen crater in the northeast of VK based on in-situ visible and near-infrared spectral observations of the Yutu-2 rover (Gou et al., 2020; Lin et al., 2020) (Figure S1c). The empirical model also predicts that the thickness of ejecta deposits from Finsen impact events is comparable to the lunar regolith stratum (the green layer in Figure 3c) (Lai et al., 2020; Yuan et al., 2021). Below the regolith layer, various scattering signals are present, along with several continuous LPR reflectors (red dash lines in Figure 3c): these horizontal features are interpreted as the base of ejecta delivered by multiple impact events (Lai et al., 2019). From the sixteenth lunar day [indicated by the red triangle in Figure 3a, the subsurface reflector (black solid line in Figure 3c)] caused by the interface between regolith and ejecta appears to rise (black triangle in Figures 3a and 3c) for a short distance at the traveling distance of 340 m then declining sharply between 380 and 480 m (between the red and green triangles in Figures 3a and 3c). After 480 m, the reflector flattens and then gradually rises again at the end of the travel path. The shape of this part of the subsurface reflector evokes the cross-section of an impact crater.

Please note that although piece-wise permittivity is adopted here for delay-depth conversion, the real permittivity varies with location and will introduce some distortion of the subsurface geometry. In Figure S3b, the boundary between the two values of permittivity is set as the subsurface reflector and marked by the black line in Figure 3c.

The geometry correction for the varying permittivity does not alter the crater-like shape but may cause some errors in estimating the slope of the crater wall.

Overall, this strong reflection boundary might represent the paleo-surface beneath the surveyed path (Figure 3c). Below this depth, several linear discontinuities suggest structural geology features, such as the “funnel”-like structure reminiscent of a flattened horst and graben region, with associated normal faults (yellow dash lines in Figure 3c). The layered structure of ejecta deposits, still visible and horizontal on the left of the image, might have been dislodged and plastically deformed by the impact event (red dashed lines in Figure 3c). It may represent the first direct evidence of the consequences of the shock effects in the lunar subsurface, i.e., faulting, fractures, and chaotic bedrock (Heggy & Paillou, 2006).

3.2. Buried Crater

The visible surface depression that lies to the southwest of the Yutu-2 rover’s travel path outlined in Figure 2 might represent the surface expression of the potential buried crater detected by the LPR onboard the rover. The contour lines and 3D view (Figures 2b and 2c) shows the shape of the depression and the relative positions of the LPR scanning line to the center of the depression. When the rover crossed the edge of the crater (black dash line in Figure 2b), the observed subsurface reflector began to fall, indicated by the red dots in Figure 2b. The distance from the rover to the depression center has a strong correlation with the topography of the subsurface reflector, illustrated by the purple line and red dash line in Figure S3. The Pearson correlation value between the two sets of data is 0.96. The correlation is relatively weak toward the end of the path because of the possible effect of another depression to the north (Figure 2c) or resulting from the modification stage of the underlying crater. Figure 2b shows that the rover only traveled along a short yet non-straight path inside the buried crater and did not cross the center, so the flat part of the subsurface reflector probably does not represent the crater floor (Figure S4). The slope of the subsurface reflector is 10°. Assuming the depression (circled by the white dash line in Figure 2a) is caused by the detected buried crater and, given its deduced size, it represents a simple bowl-shaped crater, the diameter of the buried crater can be estimated at 270 ± 10 m and the radial gradient of the slope at 29°. Considering the resolution of the surface DEM is 5 m, the range of the radial gradient is 24°–36.5°. Craters can be classified as A, AB, B, BC, C types, where A type represents the youngest impacts with walls having the steepest angle of slope and the most pristine rim morphology, while C is the most degraded (Basilevskii, 1976). Accordingly, the estimated age of the crater can be inferred based on these considerations and relating to their diameter (Basilevskii, 1976). Within this model, the buried crater would belong to either the A or AB type, and its age could be no older than 100 m.y. according to the current models of destruction rates on the lunar surface (Basilevskii, 1976; Fassett & Thomson, 2014).

Multiple scattering signals draw a detectable but fuzzy upper subsurface boundary for most of the Yutu-2 journey (red arrows in Figure 3b), but between 390 and 440 m of the accumulated travel, this turns into a strong, continuous, and sharp reflector (black arrows in Figure 3b). It suggests changes in the roughness of the interface that are consistent with the LPR scanning the parts of the buried crater wall. Rocks or a rough surface could create hyperbolic-shaped radar signals, while “smoother” impact melt plastering crater walls would produce sharp and clear reflectors (Stopar et al., 2014). To investigate further the presence of impact melt-rich deposits (Figure S5), we applied two complementary methods to obtain the permittivity values of the materials beneath the black arrows in Figure 3b. The deconvolution method estimates the permittivity value to be 6.8, and the second approach assumes the continuity of a subsurface interface and provides the range of permittivity value between 5.8 and 6.2. The permittivity value of the impact melt sample 14,310 collected in the Apollo 14 mission is 6.46 (Bassett & Shackelford, 1972), which is compatible with our estimation results. Other materials associated with the permittivity value in the range of 5.8–6.5 are breccia.

The continuous reflectors within the buried crater indicated by the green arrows in Figure 3b could have been caused by the depositing events of infilling materials or a thin ejecta layer sequence of a series of small impact events. The infilling materials include scree originating from both the crater rim and the steep walls, which accumulated on the crater floor during the degradation process, along with the landed ejecta from the Finsen crater. It also demonstrates in principle that ground-penetrating radar can reveal level or tilted layers resulting from depositional processes.

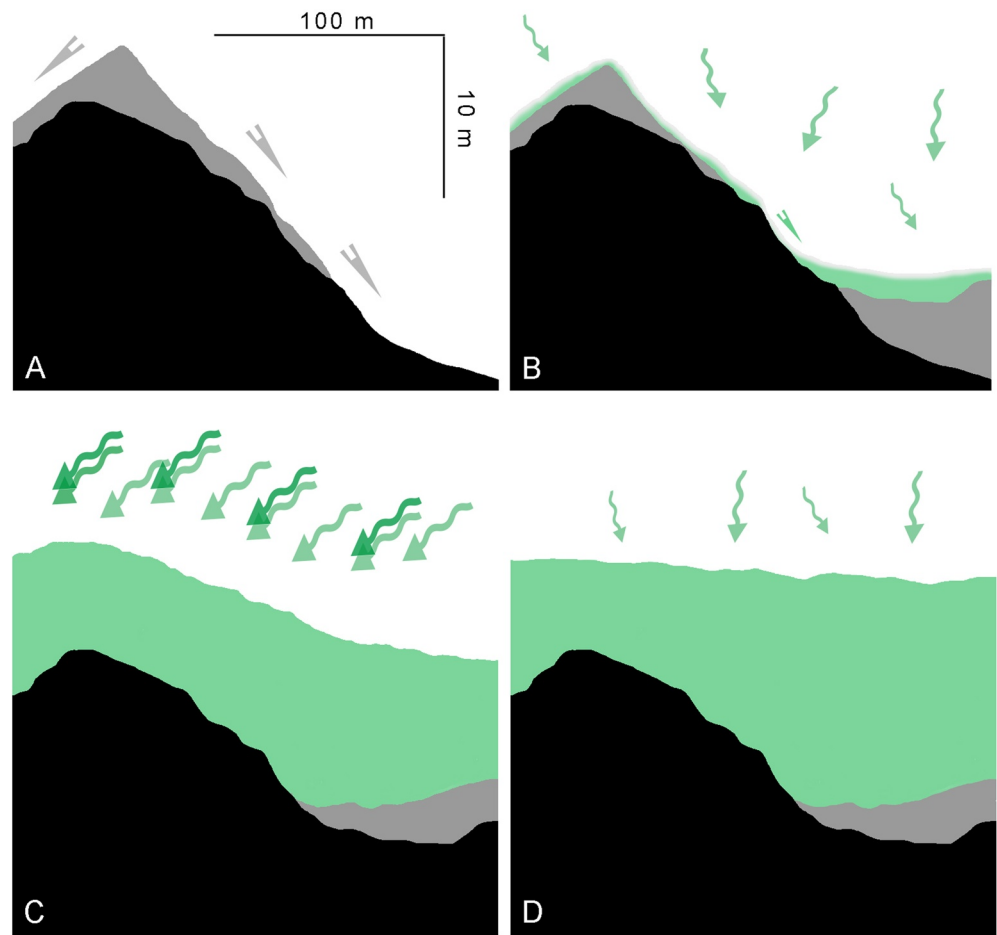


Figure 4. Conceptual model of the surface modification processes occurred at the Chang'e-4 landing site. (a) First stage: early erosional and diffusional phase; (b) Second stage: the (paleo-) surface undergoes further erosion, the effects of space weathering, and the accumulation of random ejecta material; (c) Third stage: ejecta from the Finsen impact buries the crater; (d) Fourth stage: gardening processes endure. The black color indicates the detected paleo-surface boundary; the gray color represents the gravitationally mobilized materials produced during the erosional and diffusional phase; the green parts are delivered ejecta materials.

3.3. Surface Modification

Based on the evidence from the radar signals, we propose the following geological scenario, as illustrated, and summarized in Figure 4:

(A) First stage: The exposed (paleo-) surface post-impact, featuring a fresh ~300 m crater. Through erosional and diffusive processes, the post-impact topography gradually smoothens; (B) Second stage: this process continues while scree materials accumulate, regolith forms, and impact ejecta from distal events are deposited; (C) Third stage: ejecta from the Finsen impact event arrives burying the crater, betraying its presence on the surface by a subdued ghost topography; Calculations suggest less than 100 m.y. passed between the excavation of the buried crater and the Finsen impact; and (D) Fourth stage: After surface modification of about 3.1 Ga (Lu et al., 2021), only a shallow surface depression remains visible, barely visible to the naked eye as a highly degraded crater

Gravity-led wasting, impacts and space weathering have reshaped the lunar surface profoundly. The elevation variation between the current surface and the alleged paleo-surface is 11.5 m on average, ranging from 5.8 to 17.6 m. It should be noted that the Yutu-2 rover traveling path is designed to minimize hazards, principally surface roughness and steep gradients: consequently, although radar image shows that the paleo-surface changed to a much flatter surface with average topographical variations of 1.1 m, it is not sufficient to prove that the VK crater floor before Finsen impact is much rougher than the current surface is.

Although the lunar surface was reshaped by the events described above, the paleo-surface still affects the elevation of the surface. The Pearson correlation value between the paleo-surface and the current surface of the entire traveling path is 0.89, and the value increases to 0.95 for the buried crater part. The alignment between the two surface profiles might be explained by the absence of other significant ejecta/impact events post-Finsen.

CE-4 LPR provides a unique opportunity to observe ancient lunar surfaces (“paleo-surfaces”) hidden by the ubiquitous regolith layer (ranging from 7 to 20 m, depending on location) which could, as in this case, differ substantially from the visible interface. Also, the location of a paleo-surface could represent a target for a future exploration mission trying to study the space environment, like solar activity levels, at the time of burial (Crawford et al., 2021).

A 270 m sized buried crater is identified and show that the corresponding highly degraded crater on the surface might represent the depression originating from the underlying structure, which has important implications for future crater geomorphic studies and crater statistical analysis. LPR also demonstrates its capability to capture the features of middle-small scale craters, and level/tilt reflectors resulted from previous depositions as references for future lunar, Martian, or asteroids’ missions.

4. Conclusions

The lunar surface bears witness to billions of years of astrophysical phenomena within the solar system and the study of impact craters represents the most important tool in decoding its complex geologic history (e.g., Hartmann, 1970).

The ground-penetrating radar (LPR) on the Yutu-2 rover of Change-4 (CE-4) mission has been surveying the lunar farside since the beginning of 2019. In this paper, we report the first 25 lunar days of LPR data revealing a complex ancient lunar surface (paleo-surface), the elevation profile of which has been substantially modified after about 3.1 billion years since formation. For the first time, the LPR has mapped a 270 m sized buried crater resembling a highly degraded crater as seen on the lunar surface. The geomorphology, the subsurface structure affected by the shock wave, the impact melt deposits, and the derived exposed time of the crater, are analyzed in the paper.

Previous publications on CE-4 LPR results mainly focus on the layered subsurface structure of the CE-4 surveying area and corresponding geologic history. However, this paper offers a different perspective from prior LPR results by showing the paleo-surface of the lunar farside at the depth of 12 m and the first mapping of the clear profile of a buried crater that had not been mentioned or discussed in other related work. The significance of the findings is high: although other missions have found large-scale buried craters on both Mars and the Moon, our results are outstanding in terms of data resolution and accuracy.

Data Availability Statement

CE-4 LPR data are available at Data Publishing and Information Service System of China’s Lunar Exploration Program (https://moon.bao.ac.cn/ce5web/searchOrder_dataSearchData.search). All the LPR data IDs are listed in Table S1. The data sources of Figure 2 are available in Robinson et al. (2010) and Robinson (2019).

References

- Basilevskii, A. T. (1976). On the evolution rate of small lunar craters. *The Lunar and Planetary Science Conference, 1*, 1005–1020.
- Bassett, H. L., & Shackelford, R. G. (1972). Dielectric properties of Apollo 14 lunar samples at microwave and millimeter wavelengths. *Lunar and Planetary Science Conference Proceedings* (Vol. 3, p. 3157).
- Carrier, W. D., Olhoeft, G. R., & Mendell, W. (1991). Physical Properties of the Lunar Surface. *Lunar Sourcebook*, 522–530.
- Crawford, I. A., Joy, K. H., Pasckert, J. H., & Hiesinger, H. (2021). The lunar surface as a recorder of astrophysical processes. *Philosophical Transactions of the Royal Society A: Mathematical Physical and Engineering Sciences*, 379, 20190562. <https://doi.org/10.1098/rsta.2019.0562>
- Evans, A. J., Soderblom, J. M., Andrews-Hanna, J. C., Solomon, S. C., & Zuber, M. T. (2016). Identification of buried lunar impact craters from GRAIL data and implications for the nearside maria. *Geophysical Research Letters*, 43, 2445–2455. <https://doi.org/10.1002/2015gl067394>
- Fang, G. Y., Zhou, B., Ji, Y. C., Zhang, Q. Y., Shen, S. X., Li, Y. X., et al. (2014). Lunar Penetrating Radar onboard the Chang'e-3 mission. *Research in Astronomy and Astrophysics*, 14(12), 1607–1622. <https://doi.org/10.1088/1674-4527/14/12/009>
- Fassett, C. I., & Thomson, B. J. (2014). Crater degradation on the lunar maria: Topographic diffusion and the rate of erosion on the Moon. *Journal of Geophysical Research: Planets*, 119(10), 2255–2271. <https://doi.org/10.1002/2014je004698>
- Goldberg, D. (1991). Real-coded Genetic Algorithms, Virtual Alphabets, and Blocking. *Complex Systems*, 5.

Acknowledgments

Scientific data are provided by the China National Space Administration (CNSA). We are grateful for the support from the team members of the Ground Application and Research System (GRAS), who contributed to data receiving and preprocessing. We are grateful for the constructive suggestions of two anonymous reviewers. This study is supported by the Science and Technology Development Fund (FDCT) of Macau (Grants 0042/2018/A2, 0089/2018/A3, 0079/2019/A2, and 0049/2020/A1), The National Natural Science Foundation of China, Grant number 12103020, the Pre-research Project on Civil Aerospace Technologies of CNSA (D020101), the Science and technology project of Jiangxi education department (Grant GJJ200821) and the Scientific Research Starting Foundation for scholars from Jiangxi University of Science and Technology (Grant jxxjbs18017).

- Gou, S., Yue, Z., Di, K., Wang, J., Wan, W., Liu, Z. et al. (2020). Impact melt breccia and surrounding regolith measured by Chang'e-4 rover. *Earth and Planetary Science Letters*, 544, 116378. <https://doi.org/10.1016/j.epsl.2020.116378>
- Guo, D., Fa, W., Zeng, X., Du, J., & Liu, J. (2021). Geochemistry of the Von Kármán crater floor and thickness of the non-mare ejecta over the Chang'e-4 landing area. *Icarus*, 359, 114327. <https://doi.org/10.1016/j.icarus.2021.114327>
- Hartmann, W. K. (1970). Lunar cratering chronology. *Icarus*, 13(2), 299–301. [https://doi.org/10.1016/0019-1035\(70\)90059-x](https://doi.org/10.1016/0019-1035(70)90059-x)
- Heggy, E., & Paillou, P. (2006). Probing structural elements of small buried craters using ground-penetrating radar in the southwestern Egyptian desert: Implications for Mars shallow sounding. *Geophysical Research Letters*, 33(5). <https://doi.org/10.1029/2005gl024263>
- Holland, J. H. (1992). *Adaptation in natural and artificial systems: An introductory analysis with applications to biology, control, and artificial intelligence*. MIT press.
- Huang, J., Xiao, Z., Flahaut, J., Martinot, M., Head, J., Xiao, X., et al. (2018). Geological characteristics of Von Kármán crater, northwestern south pole-Aitken Basin: Chang'E-4 landing site region. *Journal of Geophysical Research: Planets*, 123(7), 1684–1700. <https://doi.org/10.1029/2018je005577>
- Lai, J., Xu, Y., Bugiolacchi, R., Meng, X., Xiao, L., Xie, M., & Xu, L. (2020). First look by the Yutu-2 rover at the deep subsurface structure at the lunar farside. *Nature Communications*, 11(1), 1–9. <https://doi.org/10.1038/s41467-020-17262-w>
- Lai, J., Xu, Y., Zhang, X., Xiao, L., Yan, Q., Meng, X., et al. (2019). Comparison of dielectric properties and structure of lunar regolith at Chang'e-3 and Chang'e-4 landing sites revealed by ground-penetrating radar. *Geophysical Research Letters*, 46(22), 12783–12793. <https://doi.org/10.1029/2019GL084458>
- Li, C., Su, Y., Pettinelli, E., Xing, S., Ding, C., Liu, J., & Zhang, H. (2020). The Moon's farside shallow subsurface structure was unveiled by Chang'E-4 Lunar Penetrating Radar. *Science Advances*, 6(9), eaay6898. <https://doi.org/10.1126/sciadv.aay6898>
- Lin, H., Lin, Y., Yang, W., He, Z., Hu, S., Wei, Y., & Zou, Y. (2020). New insight into lunar regolith-forming processes by the lunar rover Yutu-2. *Geophysical Research Letters*, 47(14), e2020GL087949. <https://doi.org/10.1029/2020gl087949>
- Lu, Y., Wu, Y., Michael, G. G., Ma, J., Cai, W., & Qin, N. (2021). Chronological sequence of Chang'E-4 landing zone within Von Kármán crater. *Icarus*, 354, 114086. <https://doi.org/10.1016/j.icarus.2020.114086>
- Putzig, N. E., Smith, I. B., Perry, M. R., Foss, F. J., II, Campbell, B. A., Phillips, R. J., & Seu, R. (2018). Three-dimensional radar imaging of structures and craters in the Martian polar caps. *Icarus*, 308, 138–147. <https://doi.org/10.1016/j.icarus.2017.09.023>
- Qiao, L., Ling, Z., Fu, X., & Li, B. (2019). Geological characterization of the Chang'e-4 landing area on the lunar farside. *Icarus*, 333, 37–51. <https://doi.org/10.1016/j.icarus.2019.05.029>
- Robinson, E. A. (1985). Seismic time-invariant convolutional model. *Geophysics*, 50(12), 2742–2751. <https://doi.org/10.1190/1.1441894>
- Robinson, M. (2019). *Topographic Map of the Chang'e 4 Site*. Retrieved from <http://www.lroc.asu.edu/posts/1100>
- Robinson, M. S., Brylow, S. M., Tschimmel, M., Humm, D., Lawrence, S. J., Thomas, P. C., et al. (2010). Lunar reconnaissance orbiter camera (LROC) instrument overview. *Space Science Reviews*, 150(1–4), 81–124. https://doi.org/10.1007/978-1-4419-6391-8_6
- Sood, R., Chappaz, L., Melosh, H. J., Howell, K. C., Milbury, C., Blair, D. M., & Zuber, M. T. (2017). Detection and characterization of buried lunar craters with GRAIL data. *Icarus*, 289, 157–172. <https://doi.org/10.1016/j.icarus.2017.02.013>
- Stopar, J. D., Hawke, B. R., Robinson, M. S., Denevi, B. W., Giguere, T. A., & Koeber, S. D. (2014). Occurrence and mechanisms of impact melt emplacement at small lunar craters. *Icarus*, 243, 337–357. <https://doi.org/10.1016/j.icarus.2014.08.011>
- Xia, J., Franseen, E. K., Miller, R. D., & Weis, T. V. (2004). Application of deterministic deconvolution of ground-penetrating radar data in a study of carbonate strata. *Journal of Applied Geophysics*, 56(3), 213–229. [https://doi.org/10.1016/s0926-9851\(04\)00054-0](https://doi.org/10.1016/s0926-9851(04)00054-0)
- Xiao, Z., Ding, C., Xie, M., Cai, Y., Cui, J., Zhang, K., & Wang, J. (2021). Ejecta From the Orientale Basin at the Chang'E-4 Landing Site. *Geophysical Research Letters*, 48(3), e2020GL090935. <https://doi.org/10.1029/2020gl090935>
- Xu, L., Zhang, X., Qiao, L., & Lai, J. (2021). Evaluating the thickness and stratigraphy of Ejecta materials at the Chang'e-4 landing site. *The Astronomical Journal*, 162(1), 29. <https://doi.org/10.3847/1538-3881/abf8b0>
- Yang, C., Qian, Q., Wang, F., & Sun, M. (2016). An improved adaptive genetic algorithm for function optimization. In *2016 IEEE International Conference on Information and Automation (ICIA)* (pp. 675–680). IEEE. <https://doi.org/10.1109/icinfa.2016.7831905>
- Yilmaz, Ö. (2001). Processing, inversion, and interpretation of seismic data. *Seismic Data Analysis*, 231–233.
- Yuan, Y., Zhu, P., Xiao, L., Huang, J., Garnero, E. J., Deng, J., & Li, W. (2021). Intermittent volcanic activity detected in the Von Kármán crater on the farside of the Moon. *Earth and Planetary Science Letters*, 569, 117062. <https://doi.org/10.1016/j.epsl.2021.117062>
- Zhang, J., Zhou, B., Lin, Y., Zhu, M. H., Song, H., Dong, Z., et al. (2021). Lunar regolith and substructure at Chang'E-4 landing site in the South Pole-Aitken basin. *Nature Astronomy*, 5(1), 25–30. <https://doi.org/10.1038/s41550-020-1197-x>
- Zhang, L., Li, J., Zeng, Z., Xu, Y., Liu, C., & Chen, S. (2020). Stratigraphy of the Von Kármán crater based on Chang'E-4 lunar penetrating radar data. *Geophysical Research Letters*, 47(15), e2020GL088680. <https://doi.org/10.1029/2020gl088680>
- Zhang, L., Xu, Y., Bugiolacchi, R., Hu, B., Liu, C., Lai, J., & Huo, Z. (2021). Rock abundance and evolution of the shallow stratum on Chang'e-4 landing site unveiled by lunar penetrating radar data. *Earth and Planetary Science Letters*, 564, 116912. <https://doi.org/10.1016/j.epsl.2021.116912>